Landslides (2017) 14:1375–1387
DOI 10.1007/s10346-016-0794-3
Received: 15 June 2016
Accepted: 28 December 2016
Published online: 4 February 2017

C. W. W. Ng · C. E. Choi · G. R. Goodwin · W. W. Cheung

Interaction between dry granular flow and deflectors

Abstract The application of seawall deflectors for reflecting inviscid waves into the sea have been well established. Recently, rigid barrier deflectors have been proposed prescriptively for mitigating geophysical landslides, but flow characteristics differ fundamentally from waves and merit investigation. In this study, flume tests were used to calibrate a discrete element model to explore the interaction between dry granular flow and rigid barrier deflectors. The deflector angle and length and the effective height (distance between deflector tip and channel base) were studied and compared to barriers without deflectors. Findings reveal that deflectors initially prevent spilling of vertical runup and reduce flow energy underneath the deflector. However, controlling overflow depends heavily on the deflector angle and length, with the effective height as ultimate governing parameter. The additional height provided by the deflector should therefore be considered as part of the design height rather than a prescriptive add-on. Longer deflector lengths shield deadzones from energy losses through grain shearing, thus resulting in higher peak overflow velocities. It is recommended that deflector lengths should be less than 10% of the expected flow depth to suppress peak overflow velocities. Perpendicular deflectors tend to enhance faster energy dissipation through increased deadzone confining stress.

Keywords Deflector · Dry granular flow · Flume modelling · Geophysical flows

Introduction

Wave return walls are commonly installed along the coast to reduce the risk of flooding during intense storms. Such walls generally include a recurve or deflector (hereafter referred to as a deflector) detailed at the top of the wall to reduce overtopping by reflecting waves back towards the sea. The effectiveness of such deflectors can be characterised using a reduction factor k (Owen and Steele 1991; Juhl 1992; Verwaest et al. 2010) which is given as follows:

$$k = \frac{q_r}{q_c} \quad (1)$$

where q_r and q_c are the discharges overtopping the wall with and without a deflector, respectively. Kortenhaus et al. (2001) carried out experiments of waves overtopping walls and report that the freeboard R_c normalised by the wave height h should be greater than 1.3. Furthermore, Cornett et al. (1999) carried out experiments on deflectors and overtopping, reporting that deflectors at 30° from the vertical inclined towards the sea can provide discharge reduction factors of up to 10 for water.

Likewise, deflectors are also recommended for intercepting flow-type landslides (Hungr 2014). However, guidelines from wave deflectors cannot be directly applied to landslide barriers since there exist fundamental differences between the impact dynamics of materials. Wave-structure interaction is dominated by viscous and inertial forces, limited change in density upon impact (Choi et al. 2015), and structures sustain repeated wave impacts. By contrast, flow-type landslides are frictional (Iverson 1997) and tend to pile up in front of obstacles. The ramp-like deposit eventually facilitates overflow (Gray et al. 2003; Choi et al. 2014a; Ng et al. 2014).

Consequently, although recommendations are proposed for installing deflectors on top of rigid barriers to control vertical runup, interaction of flow-type landslides with such structures is still not well understood, and deflectors are not optimised for this case. For example, GEO (2012) recommends either an inclined deflector at 45° (Fig. 1a) or a curved deflector installed perpendicular to the rigid barrier (Fig. 1b), the design contrasting with that suggested by Berkeley-Thorn and Roberts (1981) for controlling waves (Fig. 1c). The recommended horizontal length L of the deflectors is $L \geq h_{max}$, where h_{max} is the maximum approach debris thickness. There is no limit on the deflector length of provided recommendations, implying that longer deflectors are more suitable for all loading cases. Furthermore, the deflectors are proposed as prescriptive measures only, meaning that any additional retention height provided by the deflector is not considered in design. Systematic research is thus merited.

Choi et al. (2016) carried out a preliminary series of small-scale flume experiments to study dry granular flow interaction with deflectors of varying angles. Results reveal that deflector angles less than 30° with respect to the horizontal plane resulted in adverse overflow conditions. However, the overall barrier height was not held constant; thus, the deflector angle was changed together with the barrier height. Furthermore, the influence of the deflector length can influence flow kinematics, but was not considered. In this study, reliable physical test data from three small-scale flume test modelling dry sand flow interaction with deflectors was used to calibrate a discrete element method (DEM) model. The advantage of the DEM model lies in its ability to characterise the flow energy spatially during the flow-deflector interaction. The calibrated DEM model is then used to study a wide range of barrier and deflector geometries including deflector length and effective height.

Numerical investigations of flow-structure interaction commonly apply depth-averaged continuum models (Savage 1984; Hungr 1995), the DEM (Chiou et al. 2005; Teufelsbauer et al. 2009, 2011), or a combination of the computational fluid dynamics and the DEM (Zhao and Shan 2013). Although depth-averaged continuum models are computationally efficient, they neglect the shear rates along the depth of the flow. However, impact is strongly influenced by the shear profile of the flow (Yang et al. 2012). DEM has been used for modelling interaction between dry granular flows and structures (Teufelsbauer et al. 2009, 2011); although there are practical constraints on the number of particles that can be simulated, it can simulate realistic shear profiles and discrete flow behaviour. CFD-DEM modelling uses a combination of the

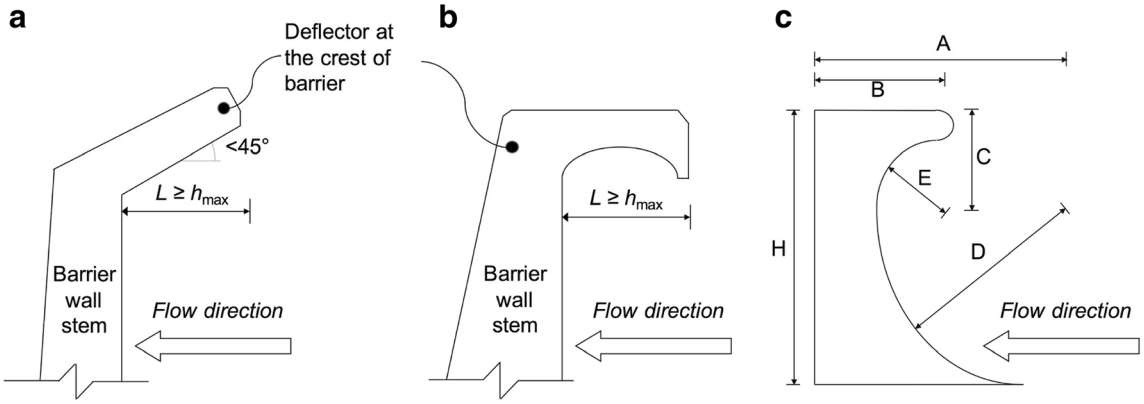

Fig. 1 Debris-flow deflector (GEO 2012) and wave-deflector design recommendations (Berkeley-Thorn and Roberts 1981): **a** inclined; **b** orthogonal; **c** curved wave-deflector

discrete element method, representing the solid phase and either computational fluid dynamics (CFD) (Zhao and Shan 2013; Shan and Zhao 2014). However, for dry flows, the air phase does not have a substantial impact on macroscopic flow dynamics (Teufelsbauer et al. 2009); therefore, DEM is sufficient for modelling dry granular flows.

Scaling

Armanini et al. (2014) proposed a two-dimensional heuristic model to characterise the rheology for gravity-driven granular flows. The coexisting collisional and frictional regimes depend on geometric and kinematic parameters dependent on Froude similarity. Furthermore, Armanini (2015) identified key dimensionless groups for gravity-driven hyper-concentrated flows. The depth average velocity of the heuristic model is given as follows:

$$U = \frac{2}{5}\frac{h}{\lambda d_p}\sqrt{\frac{\rho_w}{\rho_s}\frac{1+\Delta C}{\alpha \sin\phi} g h \sin\alpha} \quad (2)$$

where α is the channel inclination and ϕ is the friction angle, ρ_w/ρ_s is the density ratio of the fluid and solid phases, $\Delta$is the relative submerged density of the particles, λ is the linear concentration, C is the depth-averaged volume concentration and d_p is the characteristic grain diameter.

Geometric similarity with prototype flows is described using two concentration parameters (the linear concentration λ and the depth-averaged volume concentration C), as well as the dimensionless ratio of flow depth to grain size h/d_p. The Froude number N_{Fr} governs the dynamic behaviour for open channel flow and represents the ratio of bulk inertial to gravitational forces. Hübl et al. (2009) and Armanini et al. (2011) both identified N_{Fr} as a key dimensionless parameter for scaling debris-structure interaction, further validating its significance. It is necessary to achieve dynamic similarity for the flow front before impact. Dynamic similarity is achieved using the Froude number, which governs the dynamics of open channel flow. It is reported that natural geophysical flows have Froude numbers of less than five (Hübl et al. 2009; Cui et al. 2015). In order to achieve dynamic similarity, it was necessary to carry out trial experiments to determine the necessary flume configuration. After carrying out trial experiments, it was determined that an initial dry sand mass of 100 kg at an inclination of 26° developed flow fronts with a Froude number of about four in this study. The parameter h/d_p is characterised as 0.012. However, for dry granular flow, the concentration is a function of N_{Fr} and h/d_p, and so is not an independent parameter. Furthermore, the channel inclination is fixed in this study to isolate the influence of the deflector angle, whilst the friction angle of sand is a material property and is not varied.

A dimensional analysis through macroscopic and mesoscopic approaches (c.f. Iverson 2015) would also have concluded that N_{Fr}, h/d_p and the concentration are the most relevant dimensionless groups for this study (given the complex nature of the flow interaction problem in this study, local shear stress and rate are not of primary interest).

Flume modelling

Figure 2a shows the flume model used to study dry granular flow impacting a rigid barrier with a deflector, whilst Fig. 2b shows a side view schematic (Choi et al. 2015). The flume has a length of 5 m, with wall height of 0.5 m and a channel width of 0.2 m. The channel is inclinable up to 45° using a crane. The hopper at the upstream end of the flume has a volume of 0.06 m^3. The spring-loaded gate is controlled using a magnetic lock between the base of the door and the channel.

High speed imagery

A high-speed camera was used to capture the flow kinematics, enabling generation of velocity fields using particle image velocimetry (PIV) analysis (White et al. 2003; Stanier et al. 2015). The camera (Mikrotron EoSens mini2) used has a sampling rate of 200 frames per second and a resolution of 1376 × 1226 pixels. High-intensity LED lighting was mounted around the flume to provide sufficient illumination.

Test programme

A summary of the physical model tests is given in Table 1; the parameters varied in Table 1 are shown in Fig. 3. The deflector angle (α) was varied as 30°, 60° and 90° from the vertical plane. The aluminium rigid barrier for each test was 100 mm high (B),

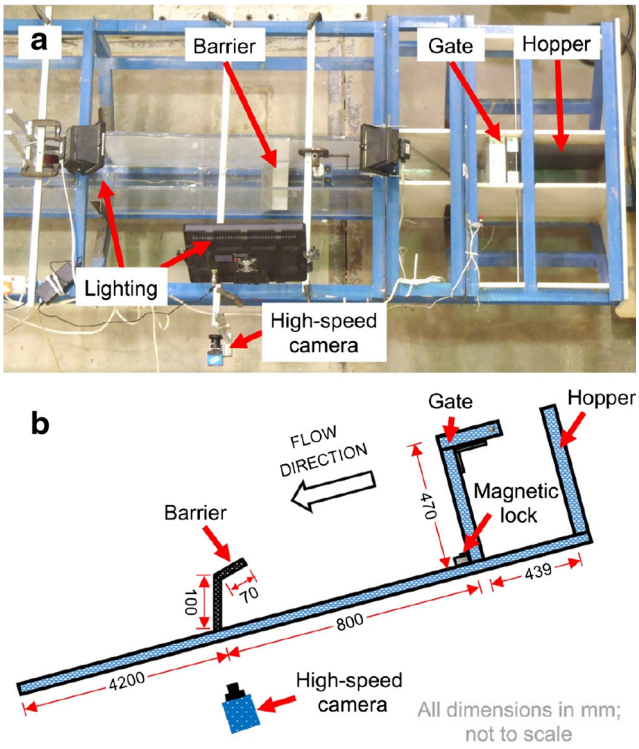

Fig. 2 **a** *Top view* of flume model; **b** *side view*

200 mm wide and 10 mm thick. The deflector was 70 mm long, which caused the equivalent deflector length (L) to vary from 35 to 70 mm. In the flume tests, the barrier height, deflector length and channel inclination (26°) were unchanged.

Model setup and testing procedures

Leighton Buzzard (LB) Fraction C sand was used for the physical tests. It is rounded and has a relatively uniform grain diameter of between 0.3 and 0.6 mm. The sand-channel interface friction angle is 22.6°. A mass of 100 kg of dry LB sand was layered into the hopper to reach a bulk density of 1680 kg/m^3. The aluminium rigid barrier and deflector were screwed into the channel 800 mm from the gate. The flume was then inclined to 26°. The hopper gate was opened remotely and was retained using a hook mechanism to avoid influencing the outflow of sand. The dry sand then flowed out of the hopper and into the rigid barrier and deflector.

Discrete element method

The DEM software "Large-scale atomic-molecular massively parallel simulator improved for general granular and granular heat transfer simulations" (hereafter abbreviated to "LIGGGHTS") was adopted to simulate the dynamics of a granular system (Kloss and Goniva 2010). The DEM is a well-established tool for tackling problems related to dry granular flows (Crosta et al. 2001; Valentino et al. 2008; Zhou and Ng 2010; Teufelsbauer et al. 2011; Ng et al. 2013; Choi et al. 2014b). In the DEM, Newton's laws of motion are used to calculate finite displacements due to forces on each particle. Each discrete element moves independently and can interact via contacts with other particles or with predefined boundaries.

Modelling dry sand with DEM entails three main limitations. Firstly, a large numbers of discrete elements are computationally demanding; so, each discrete element must be a substitute for hundreds of sand particles. The ratio h/δ for full-channelised flows for flume tests is around 175, but around 12 for DEM computations. Secondly, particle shape is spherical. Lastly, input parameters relating to basic particle motions of rolling, sliding, falling and bouncing can be difficult to quantify.

Numerical model setup

The ratio between the length scales of the physical flume experiments and numerical simulations were geometrically similar. The storage container, channel base and barriers were modelled using planar rigid walls. Only the transverse middle third of the flume was simulated for computational efficiency. A periodic boundary condition (PBC) was applied in the transverse direction to avoid unrealistic arrangements of particles at the particle-wall boundary (Rapaport 2004). A Hertzian contact model was used, comprising a spring-dashpot acting between binary contacts. Data is captured from upstream (U) and downstream (D) regions oriented parallel to the barrier (Fig. 3), which are five particle diameters (5δ) long.

Input parameters

A total of 45,000 discrete elements, 8 mm in diameter and with a particle density of 2650 kg/m^3, were used to model dry granular flow. The normal and tangential stiffness of both the particles and walls was set to 1×10^8 N/m. A coefficient of restitution of 0.5 was used, based on physical experiments (Azzoni and de Freitas 1995; Robotham et al. 1995). In dry sand flows, relative translational and rotational motions tend to be dominated by frictional contacts, so the contact friction of the discrete elements was set at 35° (Teufelsbauer et al. 2011; Chiou 2005; Law et al. 2015). To inhibit unrealistic rotations, a rolling resistance term was introduced, subjecting particles to a constant torque. The direction thereof always acts to resists relative rotations between pairs of contacting particles (Ai et al. 2011); a coefficient of 0.7 was adopted (Choi et al. 2014b). The torque between two spheres i and j in contact with each other can be expressed as follows:

$$M_r = -\left(\frac{\omega_{\text{rel}}}{|\omega_{\text{rel}}|}\right)\mu_r R_r F_n \tag{3}$$

$$\omega_{\text{rel}} = \omega_i - \omega_j \tag{4}$$

where ω_i and ω_j the are angular velocities of spheres i and j; ω_{rel} is the angular velocity between the two spheres; μ_r is the rolling friction coefficient; R_r is the discrete element radius; and F_n is the normal contact force between the particles. A summary of input parameters is given in Table 2.

Numerical simulation plan

The calibrated DEM model is used to undertake both numerical back-analyses and a parametric study. A summary of the numerical simulation plan is given in Table 3. The deflector angle and

Table 1 Flume test programme

Run ID	Angle (°)	Barrier height (mm)	Effective height (mm)	Slope (°)
A30-L2-H14	30	100	144	26
A60-L2-H11	60		105	
A90-L2-H07	90		66	

length and the effective height are varied. Other geometric and material parameters likely also affect flow-structure interaction, but given the dearth of openly available research on deflector-equipped barriers, a small subset of variables must first be focussed on.

Control tests, without deflectors, are simulated for each effective height to make a comparison between impact and overflow characteristics for cases both with and without deflectors. In the first numerical series, the deflector angle (α) is varied as, specifically 30°, 45°, 60° and 90°, whilst the barrier height (B) is held constant at 100 mm. The second series of tests investigates the effects of deflector length (L) Deflector lengths of 35, 70 and 105 mm are compared while keeping the barrier height constant. In the third series, the effective height (R_c) is investigated. The distance between the channel base and tip of the deflector is kept constant while varying the barrier height (B). Figure 3 constitutes a schematic diagram displaying the variables investigated in this study.

Numerical testing procedures

Each numerical simulation is modelled from the placement of discrete elements into the hopper to around 2 s post-impact. The particles were generated randomly within the hopper, falling to the base of the hopper under the influence of gravity. A bulk density of around 1650 kg/m^3 was achieved, based on a random packing ratio of spheres of 0.6, which is within the range of 1600 to 1700 kg/m^3 achieved for the physical sand experiments (Choi 2013). After generating the particles, the flume is inclined to 26°. The hopper gate is then deleted, and the particles flow out and interact with the barrier and deflector.

DEM model calibration

Flow processes from flume experiments

It is essential to ensure that input parameters and assumptions made in the numerical model are appropriate for simulating the

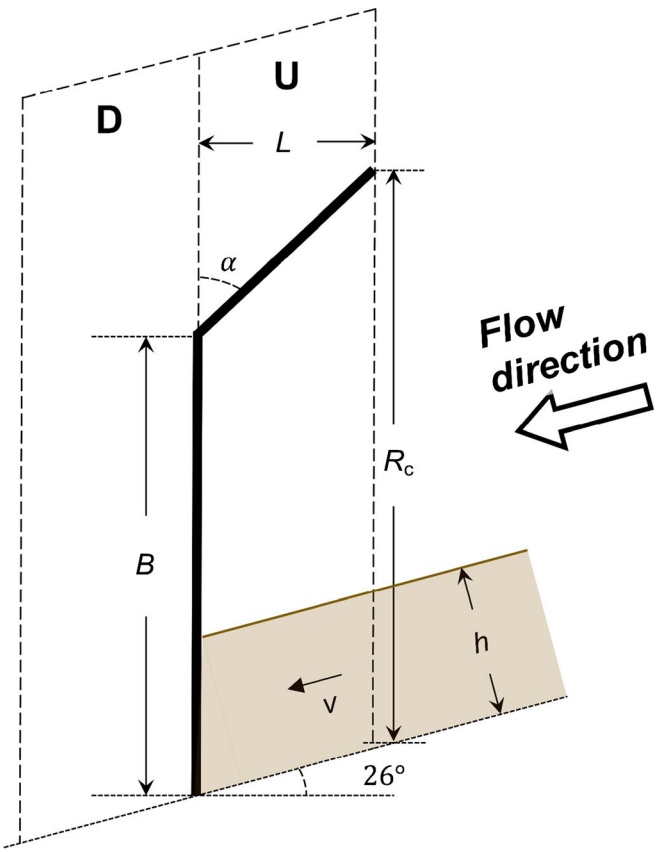

Fig. 3 Schematic of deflector variables, where B is barrier height, L is effective deflector length, v is flow velocity, h is flow depth, α is deflector angle and R_C is effective height

Table 2 DEM input parameters

Parameter (units)	Value
Number of discrete elements	40,000
Particle diameter (mm)	8
Normal and tangential particle stiffness (N/m)	1×10^8
Inter-particle friction (°)	35
Interface friction (°)	22.6
Gravitational acceleration (m/s^2)	9.8
Coefficient of restitution	0.5
Particle density (kg/m^3)	2650

kinematics of the dry granular flows impacting physical barriers before carrying out numerical investigations.

Figure 4 shows a comparison between data observed from physical tests and computed results over 0.4 s for an orthogonal (90°) deflector (test A90-L07-H07). The granular material moves towards the barrier as a wedge; the initial frontal velocity is about 2.6 m/s (Fig. 4a). The granular material impacts the barrier and starts to become deposited underneath the deflector (Fig. 4b). After the region beneath the deflector has filled up, a ramp-like deposit forms (Hákonardóttir et al. 2003; Choi et al. 2014a), bounded by the tip of the deflector. Subsequent approaching granular flow then rides over the ramp-like deposit (Fig. 4c). The overflow thickens as it cascades over the barrier downstream (Fig. 4d) and eventually impacts the base of the channel (Kwan et al. 2015) downstream of the barrier (Fig. 4e, f). The computed overflow is a little thicker than the flume tests, which is likely due to the computed particle size being larger than that adopted in the physical experiments, leading to a more inertial flow regime (discussed later) and a higher overflow discharge. Additionally, it can be seen from the flume experiments that dry sand exhibits a clear curvature as it overflows, which is not observed in the DEM simulations since no air phase is modelled in the present study: Börzsönyi and Ecke (2006) performed flume experiments using dry granular flows with and without a vacuum, demonstrating that such curvature is mainly caused by air drag.

The shear profile of a granular flow vitally influences impact dynamics (Yang et al. 2012). A sensitivity study was therefore performed to ensure that the particle size adopted did not substantially affect the shear profile in this study. Uniform particles of a particular size were placed in a channel 1.2 m in length with periodic boundaries in the planes perpendicular to the channel base. The depth of the particles was approximately equal to that of the flow depth pre-impact, i.e. 80 mm. After the particles had come to rest, the direction of gravity was altered to simulate a channel inclination of 26°. The particles then started to flow down the channel and were allowed to flow until they reached a terminal velocity. The mean velocity of the flow as a function of depth was then extracted at this terminal velocity.

Figure 5 shows the mean velocity of the flow normalised by the maximum velocity on the x-axis and vertical position on the y-axis. Several lines are plotted on the graph corresponding to different particle sizes. Consistent with granular shear profiles reported by Zhou and Ng (2010), the velocity is lowest near the bottom of the flow and increases rapidly further up. As particle size decreases, the boundary layer diminishes vertically; when the particle diameter is around 8 mm, the shear profiles converged. This gives confidence to the assumption that particle size adopted in this study is appropriate and the numerical model can capture dynamics of much smaller particles.

There are limitations in precisely capturing the flow kinematics using the DEM. In particular, physical sand grains are represented as spherical grain clusters with the same internal and interface friction angles. It should be noted that using the DEM to back-analyse granular flows is to capture shear profiles and discrete particle behaviour, which cannot be captured using other methods such as the depth-averaged method. The computed kinematics appear to reasonably capture the kinematics observed from the flume tests. A comparison of DEM models for sand flume experiments is summarised in Table 4. This exercise assures that the input parameters and model simplifications are appropriate to bear further insight into flow-deflector interaction.

Interpretation of results

Energy characteristics of flow interaction

Figure 6 shows the energy characteristics of the flow during the impact process in region U (Fig. 3), adjacent to the barrier. The kinetic energy at each instant is calculated as a summation of the kinetic energies of all the particles in that region, for both cases with and without deflectors. The total energy at each instant for cases with deflectors is normalised by the energy without deflectors, but with the same effective height. The characteristics of 30°, 60° and orthogonal deflectors are compared.

It is observed that to start with there is little difference in flow kinetic energy between cases with and without deflectors. The initial kinetic energy profiles are almost identical because the test conditions, including the initial packing arrangement for the each case, are the same. Granular runup up to the deflector is identical. At around $t = 0.44$ s, for the orthogonal (90°) deflector, the kinetic energy drops rapidly post-impact. After the rapid energy loss, the granular flow kinetics rapidly increase as overflow commences and is consistent with the kinetic energy behaviour for a rigid barrier as reported by Law et al. (2015). This corresponds to an almost complete arrest of the grains directly under the deflector. The 30° and 60° deflectors show similar kinematics, although the steep drop in kinetic energy for the case with the deflector commences slightly after the 90° case. This may be attributed to a comparative lack of confinement underneath the barrier (discussed later). Additionally, the trough representing the arrest of material is more prolonged, due to the larger volume available for retention of material.

Furthermore, the presence of a deflector is not able to effectively control the flow energy during overflow: the energy ratio remains around unity after overflow commences, reaching a peak of around 1.15 for these cases. This suggests that although deflectors are initially able to effectively mitigate runup, their performance may be worse than a simple vertical barrier which has the same effective height on the condition that there is sufficient impacting material to lead to significant overflow.

Deadzone formation

Figure 7a–c compares the deadzone formation using PIV analysis from flume tests and the computed flow kinematics from the DEM

Table 3 Numerical simulation plan

Series	Run ID	Angle α (°)	Deflector length L (mm)	Barrier height B (mm)	Effective height (mm)
Control tests (no deflector)	C-H[a]	-	-	B^1	R_c^1
Deflector angle	A30-L07-H14	30	35	100	144
	A45-L07-H13	45	50		125
	A60-L07-H10	60	60		105
	A90-L07-H07	90	70		66
Deflector length	A30-L01-H10	30	10	88	100
	A45-L01-H10	45		95	
	A60-L01-H10	60		99	
	A75-L01-H10	75		102	
	A90-L01-H10	90		105	
	A30-L03-H10	30	35	60	
	A45-L03-H10	45		76	
	A60-L03-H10	60		90	
	A75-L03-H10	75		108	
	A90-L03-H10	90		117	
	A30-L07-H10	30	70	13	
	A45-L07-H10	45		64	
	A60-L07-H10	60		94	
	A76-L07-H10	75		115	
	A90-L07-H10	90		134	
	A45-L10-H10	45	105	46	
	A60-L10-H10	60		91	
	A75-L10-H10	75		123	
	A90-L10-H10	90		151	
Barrier height	A45-L07-H04	45	50	20	41
	A45-L07-H06			40	59
	A45-L07-H08			60	77
	A45-L07-H10			80	95
	A45-L07-H12			100	113
	A45-L07-H14			120	131
	A45-L07-H16			140	149

[a] Control tests without deflectors were carried out for each effective height

for 90°, 60° and 30° deflectors, respectively. For each of the deflector angles, the flow process is shown chronologically from top to bottom. Time begins at t = 0 s, just before the barrier is impacted by the flow front. For each PIV image, the maximum velocity (v_{max}) is shown.

The deadzones show reasonable agreement between the PIV analysis and DEM simulations as sand fills up underneath all three deflectors. However, as the deadzone extends along the upstream direction, the DEM model and PIV exhibit divergence. Differences may be attributed to the PIV analysis, which captures the velocity field of static particles which result from intense shearing between the flow of grains and side wall. This layer may not be totally representative of the deadzone along the transverse direction. Furthermore, Gollin et al. (2015) carried out a comparison of methods for physical measurements of particle flows, and it is noted that PIV tends to damp the magnitude of particle velocities. The DEM simulations adopt a PBC, and so, intense shearing is not captured along the side walls. Another fundamental reason for the variance may be the disparity in particle diameter between the flume experiments

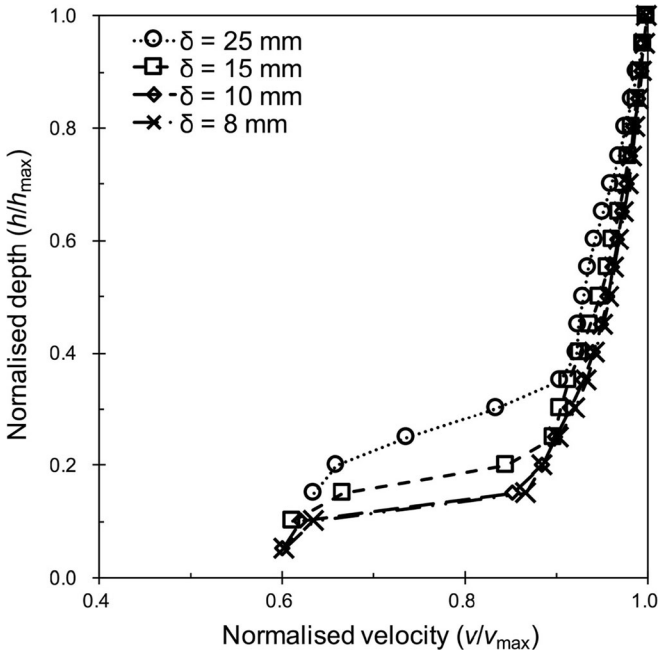

Fig. 4 Convergence study considering different particle sizes

and DEM simulations: the discrete elements are relatively more inertial, the packing arrangement is not as dense, and there are likely not as many contacts. Additionally, these highly inertial discrete elements close to the top of the deadzones are more entrained more easily by the overflow, thus influencing the deadzone geometry. This phenomenon can be investigated using the Savage number (N_{SAV}) which allows characterisation of the ratio of inertial and contact grain shear stresses (Savage 1984; Iverson 1997):

$$N_{\mathrm{Sav}} = \frac{\gamma^2 \rho_s \delta}{N\left(\rho_s - \rho_f\right) g \tan\phi'} \tag{5}$$

where γ is the shear rate; ρ_s is the solid material density; ρ_f is the fluid material density; δ is the grain diameter; N is the ratio of flow depth to characteristic grain diameter (h/δ); g is the acceleration

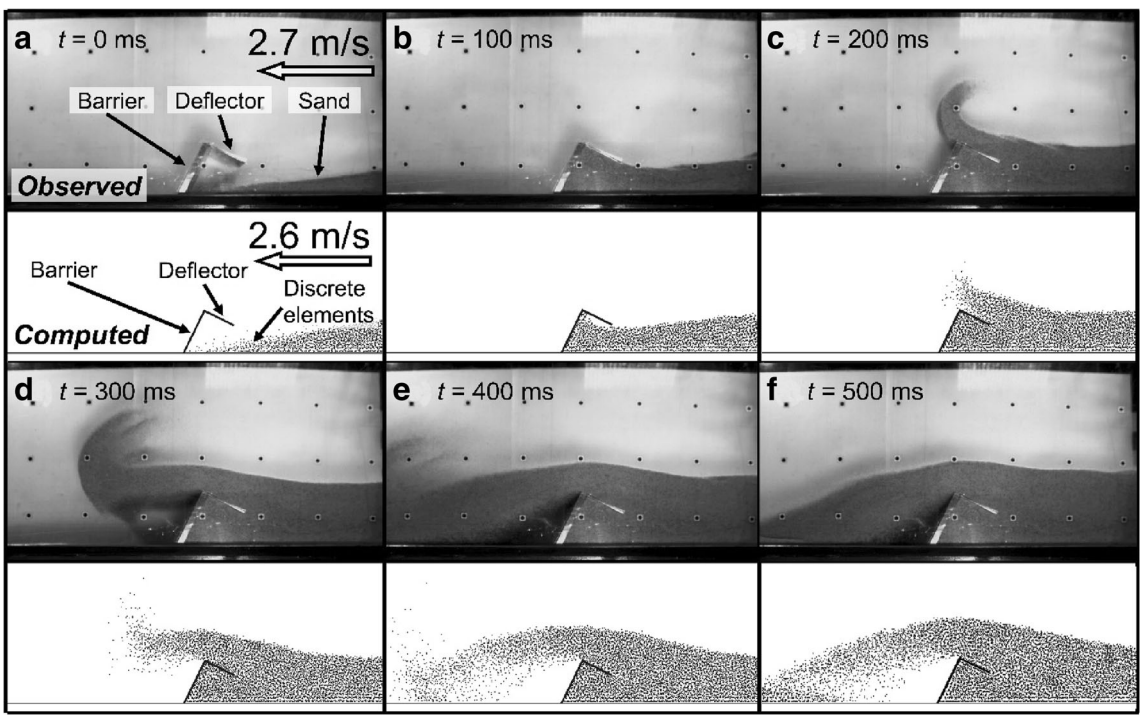

Fig. 5 Comparison of observed and computed flow dynamics (test A90-L07-H07): **a** t = 0 ms; **b** t = 100 ms; **c** t = 200 ms; **d** t = 300 ms; **e** t = 400 ms; **f** t = 500 ms

Table 4 Comparison of physical and computed particle sizes for several DEM studies.

Study	Particle size of material modelled (mm)	Particle size adopted for DEM (mm)	Number of particles	No. of dimensions
Valentino et al. 2008	0.6	1.2–1.4	19,500	2
Teufelsbauer et al. 2011	0.25	4–6	43,000	3
Choi et al. 2014b	0.3–0.6	5	65,000	3
This study	0.3–0.6	8	45,000	3

due to the Earth's gravity; and ϕ' is the effective internal friction angle of the solid material. Since the fluid density is negligible, N_{Sav} is independent of solid density, suggesting that solid density is not a controlling parameter for overflow dynamics. There is a difference of an order of magnitude between the estimated Savage numbers for the physical and computed flows. This implies that the shear rate between overflow and the deadzone layer strongly influences the entrainment of material (Hsu et al. 2008) and deadzone geometry. This is supported by a comparison of the three deflector angles: the orthogonal (90°) retains the highest overflow velocity, and hence shear rate, and has the smallest deadzones.

The physical and computed data both demonstrate that the deadzone free surface is essentially bounded by the deflector tip. For the 90° case, the deadzone encroaches onto the top of the deflector, indicating that the highest point of the structure may be a minor influence on the deadzone. Findings from the physical tests are consistent with results presented by Faug et al. (2002).

Influence of deflector angle on deadzones

Figure 8 shows a comparison of the deadzones for structures with the same effective height for $\alpha = 30°$ and 90°. $\alpha = 45°$ and 60° are not shown for clarity, but are discussed in the text. The effective height is defined as the distance between the tip of the deflector and the base of the channel (such a comparison is necessary, since given the same volume, taller barriers will undoubtedly be more effective at suppressing overflow). The x and z positions are normalised by the distance between the hopper gate and the foot of the barrier. Two deadzones are shown for each deflector angle for when $t = 0.56$ s, just after impact, and at $t = 1.7$ s when the deadzones are near full development.

At time $t = 0.56$ s, the bounds of the deadzones for deflector angles of 30°, 45° and 60° are almost the same, suggesting that a controlling factor for deadzone formation is indeed the effective height. However, it is observed that the deadzones for the 90° (test A90-H10) deflector has not completely filled the area underneath the deflector. The difference is attributed to the taller barrier height B of the 90° case. A slightly larger volume is available for debris to come to rest in, and so, it initially takes longer for the face of the deadzones to reach the tip of the deflector, above the reference line. At $t = 1.7$ s, the boundary of the deadzones for when deflectors are 30°, 45° and 60° are almost identical, with only minor variation further upstream at around $x = 0.5$. The difference in volume enclosed by the three different deflectors is not substantial enough to cause a large difference in the deadzone formation. Additionally, for these cases, grains are unable to come to rest on top of the deflector, instead sliding down onto the channel downstream. However, for the 90° deflector, both the enclosed volume is larger and the tip of the barrier is also taller than the effective height. This increases the retention capacity, because grains are eventually able to come to rest on top of the deflector.

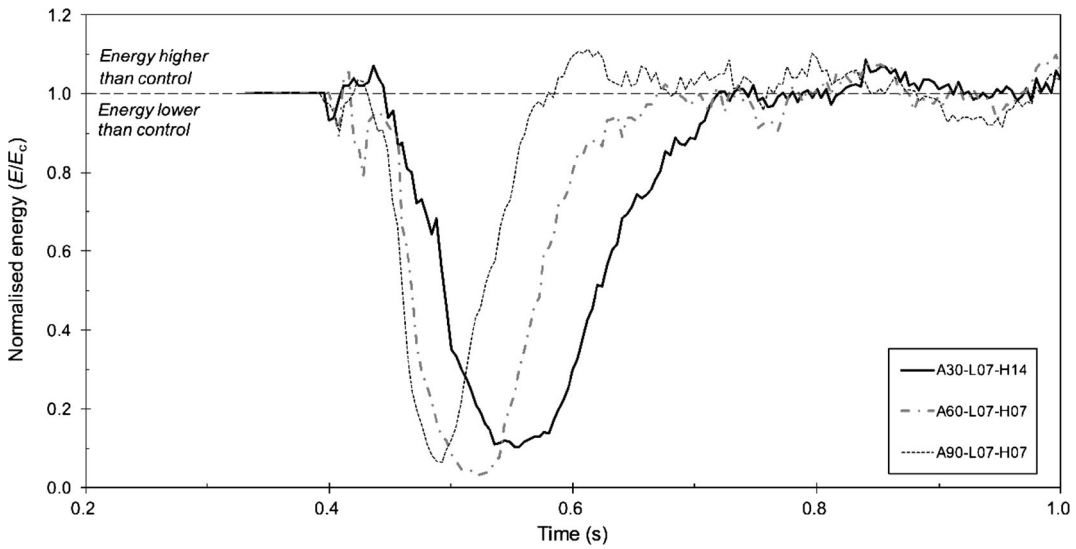

Fig. 6 Ratio between the kinetic energy in region U for flow impacting a deflector-equipped barrier (E) and a deflectorless rigid barrier (E_C) as a function of time (region U denotes a region five particle diameters long, capturing data from an area directly in front of the barrier)

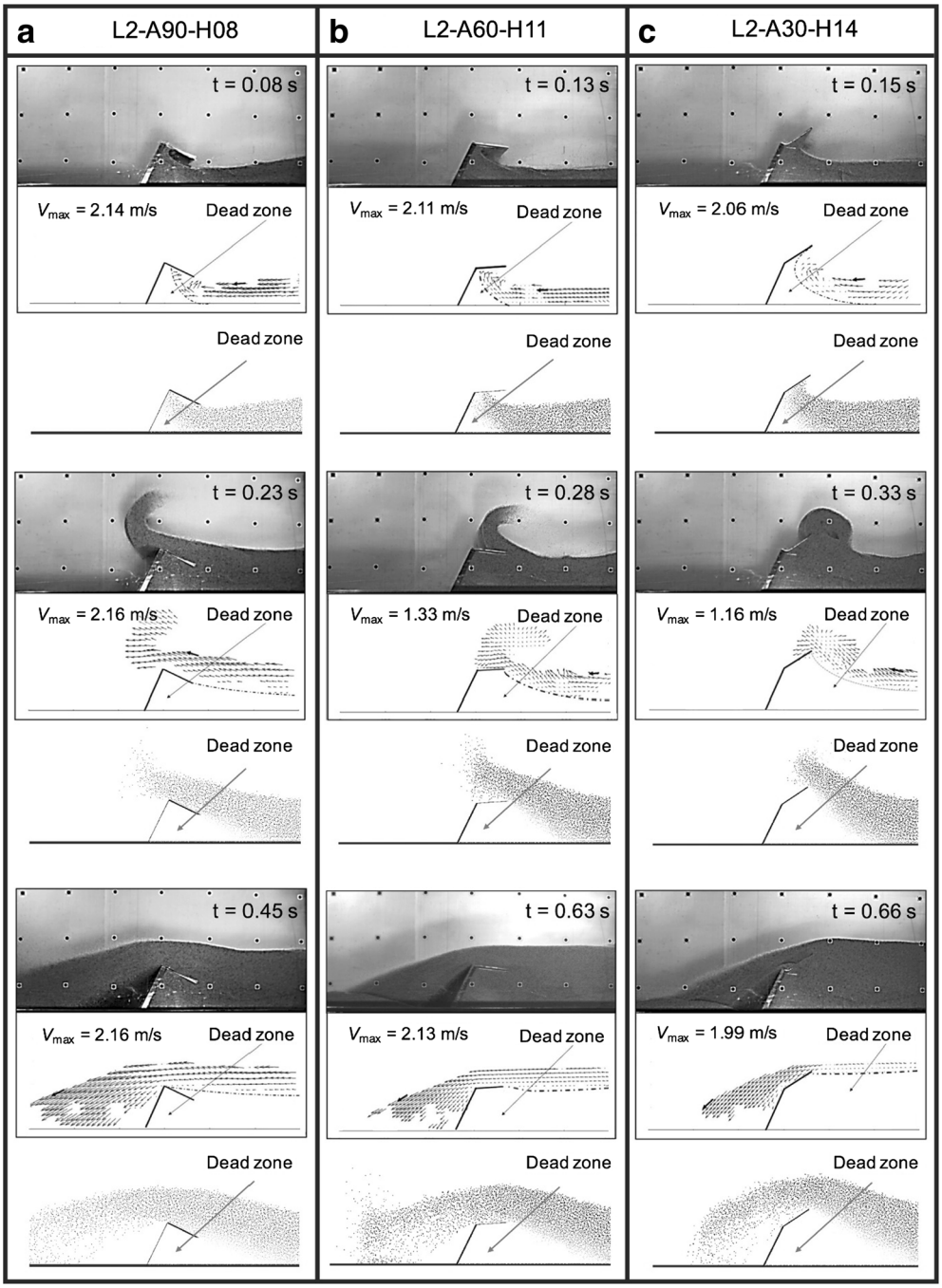

Fig. 7 Observed kinematics and PIV analysis from flume tests vs computed kinematics from DEM

A comparison of deadzone development reveals that it is the highest point of the structure above the channel base which dictates the evolution of the deadzones, and hence the volume of material retained. Faug et al. (2002) reports that the deadzones are principally a function of the channel inclination, friction angle of the granular material and obstacle Froude number which is governed by the height of the obstacles. This is in line with the observation in this study where the effective height (distance from tip of deflector to base of channel) governs the retention of granular material behind a barrier. This indicates that deflectors should be geometrically considered as part of the barrier during interaction process, rather than as a prescriptive measure (GEO 2012), as the deflector tip controls the retention of debris behind the barrier.

Influence of deflector length

Runup may translate into material overspilling, with potentially catastrophic consequences if the volume of material is larger than anticipated. Hence, it is necessary to examine overflow characteristics resulting from rigid barrier deflectors. Figure 9 shows a comparison of the peak overflow velocity ratio for deflector-

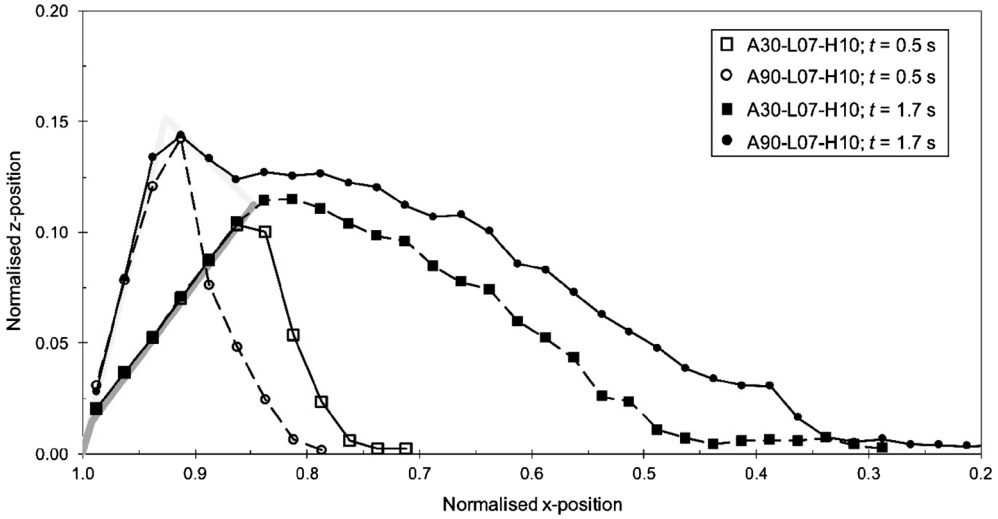

Fig. 8 Deadzone evolution for barriers of the same effective height and varying deflector angles

equipped structures which have the same effective height (R_c), but varying deflector lengths (L), and by extension varying barrier heights (B). The deflector length is normalised by the flow depth of the incoming granular flow (h). The ratio of deflector length to flow depth suggested by GEO (2012) is also shown for comparison. As far as the authors are aware, no guidelines exist for the length of wave deflectors, although limited research has been carried out by Kortenhaus et al. (2003) and Schoones (2014). The overflow velocity ratio compares the peak velocity from cases with and without deflectors; the control cases are as tall as the highest point on the deflector-equipped structures. Five deflector angles are compared: 30°, 45°, 60°, 75° and 90°. The peak overflow velocity typically corresponds to the very start of the overflow process.

For longer deflectors (i.e. L/h = 0.4, 0.9 or 1.3), the peak velocity is higher when a deflector is included. This may be attributed to the deflector shielding deadzone free-surface from shearing whilst overflow occurs. The deflector enables minimisation of overflow energy loss due to particle shearing. Between the particle and deflector plate the interface friction angle is 22.6°, whereas the inter-particle friction angle is 35°. Comparing short (L/h = 0.1 and 0.4) and long (L/h = 0.9 and 1.3) deflectors demonstratesthat longer deflector lengths cause an increase in this shielding effect. The short and long deflectors cause up to 22% increases in the peak velocity of overflowing material compared to barriers which do not have deflectors. In contrast, including a very short deflector (L/h = 0.1) in general reduces thepeak overflow velocity, since the most energetic particles at the flow front are arrested successfully during impact with the deflector, but the shielding effect becomes minimal due to the short length of the deflector. This implies that the longer deflectors designed to control runup and over-spilling that are detailed in existing guidelines (GEO 2012) have a tendency to lead to higher peak overflow velocities, suggesting that the length of deflectors should be designed to be around a tenth of that of the predicted flow depth (nonetheless maintaining control of runup). In contrast, Schoones (2014) determined that a reduction in the dimensionless mean overtopping rate is effected by a longer deflector for a particular relative freeboard. This difference in performance is attributable to the fundamental differences between loading characteristics of waves and flow-type landslides, since the latter generally pile up in front of the obstacle during a single impact event, thus tending to make them susceptible to the shielding effect described above. By contrast, waves do not have shear strength and thus have a tendency to follow the curve of a lengthened deflector back towards the sea, without a long-term reduction in the relative freeboard.

Additionally, as deflectors approach the vertical, the peak overflow velocity tends to increase for all deflector lengths. This may be attributed to the reduction in volume enclosed by the deflector: the grains near the front of the flow tend to be the most energetic, characterised by a relatively high Savage number (Zhou and Ng 2010). More grains can be accommodated under a 90° deflector than under a 30° one; so, the most energetic grains are unable to flow downstream. Thus, considering the peak overflow velocity effects for dry granular flows, short (i.e. L/h ~ 0.1), orthogonal deflectors are recommended for improved performance in overflow situations.

Deflector reduction factor

Figure 10 shows a comparison between wave return walls employed for coastal defences (Kortenhaus et al. 2003) and structures installed for mitigating dry granular flows. The influence of the freeboard ratio R_c/h a deflector's ability to suppress overflow is shown. R_c is the effective height, defined as the distance between sea level and the crest of the wave-breaking structure, or, for the present study, the distance between the channel bed and the tip of the deflector. h is the significant wave height. The minimum recommended ratio between effective height at wave height from Kortenhaus et al. (2001) is also plotted for reference. For the present study, the pre-impact flow depth h at plane U (upstream of the barrier) is used for the purposes of making comparisons and is computed to be 81 mm. For data from Kortenhaus et al. (2003), the reduction factor (k) compares the mean overtopping rate between structures with and without deflectors, respectively. For the present study, the peak overflow velocity is adopted, since there is only a single collision between debris and barrier.

Data from Kortenhaus et al. (2003) compares the performance between including and not installing a deflector on a seawall. If the ratio R_c/h is near 0 (i.e. the impacting waves are far taller

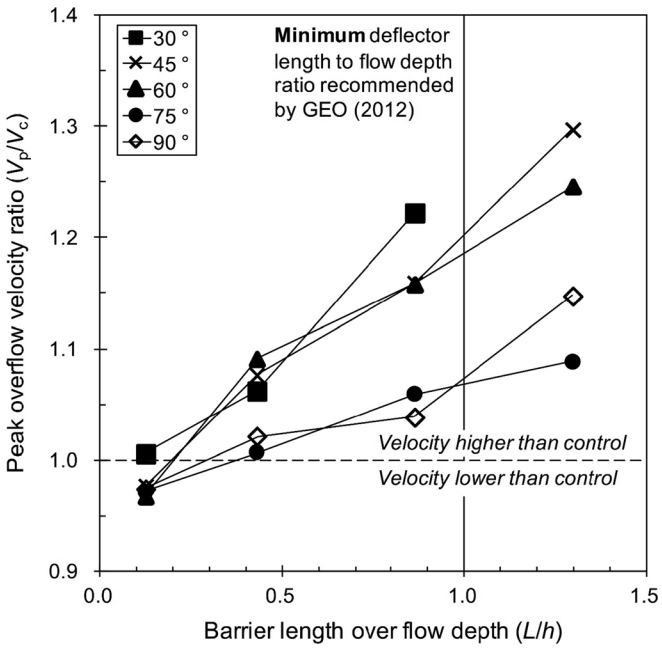

Fig. 9 Peak overflow velocity for structures with the same equivalent height, but varying barrier height; data obtained from region D (downstream)

than the seawall crest), a deflector is ineffectual at reducing overtopping. The deflector becomes 'drowned' and is unable to deflect waves back from whence they came. However, as R_c/h increases, for the range where the magnitude of the wave height and the seawall crest are comparable, k decreases. This implies that the inclusion of a deflector is able to reduce the amount of seawater overtopping a structure. For $R_c/h \geq 1.3$, deflectors completely eliminate overtopping (Kortenhaus et al. 2003). This is because water is able to energetically run up a planar surface: energy losses for channelized water flows are minimal and are due mostly to viscous shearing (Choi et al. 2015). Additionally, it is incompressible at sub-sonic velocities; so, energy cannot be expended through compression.

However, it seems that including a deflector does not make a substantial impact on the peak overflow velocity for dry granular material, which impacts a debris-resisting structure as a single surge. Most values fall in the range 0.9 to 1.1, indicating that including a deflector makes little difference, since the material modelled is frictional in nature. Granular material tends to pile up and undergo compression (Choi et al. 2015), and energy losses

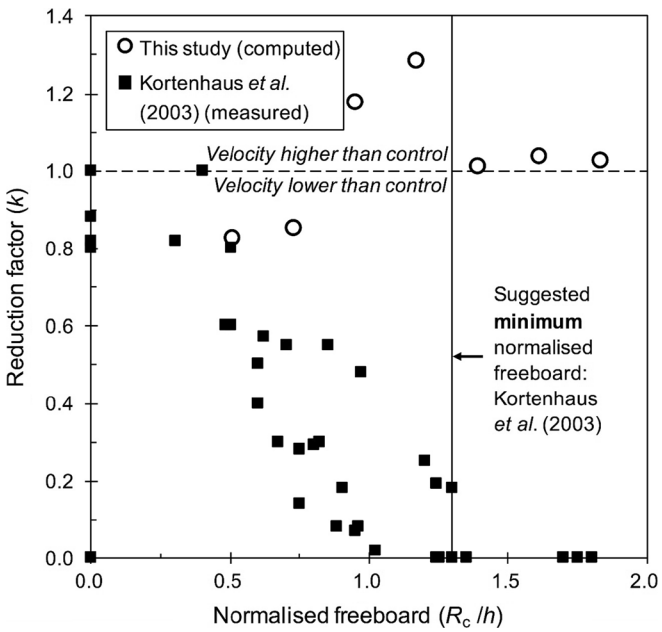

Fig. 10 Comparison between reduction factors for the DEM results in this study and water impacting a scaled seawall deflector, from Kortenhaus et al. (2003)

during runout and collision for a channelized sand flow are significant, stemming from frictional shearing and compression, which further inhibits a tendency towards energetic runup. The relative importance of potential frictional effects of the flow should thus be a consideration for barriers (Kwan et al. 2015) used to resist geophysical flows.

Conclusions

Flume tests were carried out to calibrate a discrete element model to study the interaction of dry granular flow with rigid barrier deflectors. The influences of varying the deflector length, effective height and deflector angle were investigated. Findings from this study are as follows:

a) Findings show that the prevailing design of a deflector can initially prevent spilling of vertical runup and reduce flow energy underneath the deflector. However, conditions for adverse overflow depends heavily on the effective barrier height, length and angle of the deflector
b) The deflector reduction factors (k) for dry granular flows for barriers with the same effective height are around unity regardless of deflector angle and length. This indicates that effective height is the governing parameter in the design of rigid barrier deflectors and the additional height provided by the deflector should be considered as part of the design height rather than a prescriptive add-on.
c) The inclusion of a deflector is effective at reducing flow energy directly after impact. However, in contrast to wave loading (Schoones 2014), peak overflow velocity increases with the deflector length. Longer deflector lengths shield deadzones from energy losses through grain shearing, thus resulting in higher peak overflow velocities. It is recommended that deflector lengths should be less than 10% of the expected flow depth to suppress peak overflow velocities.

Acknowledgments

The authors are grateful for financial support from research grant T22-603/15-N provided by the Research Grants Council of the Government of Hong Kong SAR, China and the HKUST Jockey Club Institute for Advanced Study for their support.

References

Ai J, Chen JF, Rotter JM, Ooi JY (2011) Assessment of rolling resistance models in discrete element simulations. Powder Technol 206(3):269–282
Armanini A, Larcher M, Odorizzi M (2011) Dynamic impact of a debris flow front against a vertical wall. In: 5th International conference on debris-flow hazards mitigation: mechanics, prediction and assessment. 14–17 June 2011. Padua, Italy, pp 1041–1049
Armanini A, Nucci E, Dumbser M (2014) Submerged granular channel flows driven by gravity. Adv Water Resour 63:1–10
Armanini A (2015) Closure relations for mobile bed debris flows in a wide range of slopes and concentrations. Adv Water Resour 81:75–83
Azzoni A, de Freitas MH (1995) Experimentally gained parameters, decisive for rock fall analysis. Rock Mech Rock Eng 28:111–124
Berkeley-Thorn R, Roberts AG (1981) Sea defence and coast protection works. Thomas Telford Ltd, London
Börzsönyi T, Ecke RE (2006) Rapid granular flows on a rough incline: phase diagram, gas transition, and effects of air drag. Phys Rev E 74:061301
Chiou, M-C (2005) Modelling of dry granular avalanches past different obstructs: numerical simulations and laboratory analyses. PhD dissertation, Technical University Darmstadt
Chiou M-C, Wang Y, Hutter K (2005) Influence of obstacles on rapid granular flows. Acta Mech 175:105–122
Choi CE (2013) Flume and discrete element investigation of granular flow mechanisms and interaction with baffles. Ph.D. thesis, Hong Kong University of Science and Technology
Choi CE, Ng CWW, Song D, Kwan JSH, Shiu HYK, Ho KKS, Koo RCH (2014a) Flume investigation of landslide debris baffles. Can Geotech J 51(5):540–533
Choi CE, Ng CWW, Song D, Law RPH, Kwan JSH, Ho KKS (2014b) A computational investigation of baffle configuration on the impedance of channelized debris flow. Can Geotech J 52(2):182–197
Choi CE, Au-Yeung SCH, Ng CWW (2015) Flume investigation of landslide granular debris and water runup mechanisms. Géotechnique Letters 5(1):28–32
Choi CE, Ng CWW, Goodwin GR, Liu H, Kwan JSH (2016) Flume investigation of the influence of rigid barrier deflector angle on dry granular overflow mechanisms. Can Geotech J 53(10):1751–1759. doi:10.1139/cgj-2015-0248
Crosta GB, Imposimato S, Roddeman DG (2001) Numerical modelling of large landslides stability and runout. Nat Hazards Earth Syst Sci 3(6):523–538
Cui P, Zeng C, Lei Y (2015) Experimental analysis on the impact force of viscous debris flow. Earth Surf Process Landf 40(12):1644–1655
Cornett A, Li Y, Budvietas A (1999) Wave overtopping at chamfered and overhanging vertical structures. In: Proceedings international workshop on natural disasters by storm waves and their reproduction in experimental basins. November 1999. Kyoto, Japan
Faug T, Lachamp P, Naaim M (2002) Experimental investigation on steady granular flows interacting with an obstacle down an inclined channel: study of the deadzones upstream from the obstacle application to interaction between dense snow avalanches and defence structures. Natural Hazards and Earth Science Systems 2:187–191
Geotechnical Engineering Office (2012) GEO report no. 270: supplementary technical guidance on design of rigid debris-resisting barriers. Geotechnical Engineering Office, Hong Kong
Gollin D, Bowman E, Shepley P (2015) Methods for the physical measurement of collisional particle flows. In: International symposium on geohazards and geomechnics, IOP Conf series: earth and environmental science 26. 10–11 September 2015. Warwick, UK
Gray JMNT, Tai YC, Noelle S (2003) Shock waves, deadzones and particle-free regions in rapid granular free-surface flows. J Fluid Mech 491:161–181
Hákonardóttir KM, Hogg AJ, Batey J, Woods AW (2003) Flying avalanches. Geophysical Review Letters 30(23):1–4
Hsu L, Dietrich WE, Sklar LS (2008) Experimental study of bedrock erosion by granular flows. J Geophys Res 113:F02001
Hübl J, Suda J, Proske D, Kaitna R, Scheidl C (2009) Debris flow impact estimation. In: Proceedings of the 11th international symposium on water management and hydraulic engineering. 1–5 September 2009. WMHE, Ohrid, pp 137–148
Hungr O (1995) A model for the runout analysis of rapid flow slides, debris flows, and avalanches. Canadian Geotechnical Journal 32(4): 610-623. doi:10.1139/t95-063
Hungr O (2014) The Varnes classification of landslide types, an update. Landslides 11(2):167–194
Iverson RM (1997) The physics of debris flows. Rev Geophys 35(3):245–296
Iverson RM (2015) Scaling and design of landslide and debris-flow experiments. Geomorphology 244:9–20
Juhl J (1992) Investigations on the effect of structural measures on wave impact forces and overtopping. In: Proc 3rd project workshop, MAST I G6-S. Hannover, Germany
Kortenhaus A, Haupt R, Oumeraci H (2001) Design aspects of vertical walls with steep foreland slopes. In: Proc Breakwaters, coastal structures and coastlines. 26–28 September 2001. ICE, London, pp 221–232
Kortenhaus A, Pearson J, Bruce T, Allsop NWH, van der Meer JW (2003) Influence of parapets and recurves on wave overtopping and wave loading of complex

vertical walls. In: Proc Coastal Structures. 26–30 August 2003. ASCE, Reston, pp 369–381
Kloss C, Goniva C (2010) LIGGGHTS - a new open source discrete element simulation software. In: Proceedings of the 5th International conference on discrete element methods, 25–26 August 2010. London, UK, pp 25–26
Kwan JSH, Koo RCH, Ng CWW (2015) Landslide mobility analysis for design of multiple-debris-resisting barriers. Can Geotech J 52(9):1345–1359
Law RPH, Choi CE, Ng CWW (2015) Discrete element investigation of the influence of debris flow baffles on rigid barrier impact. Can Geotech J 53(1):179–185. doi:10.1139/cgj-2014-0394
Ng CWW, Choi CE, Law RPH (2013) Longitudinal spreading of granular flow in trapezoidal channels. Geomorphology 194:84–93
Ng CWW, Choi CE, Song D, Kwan JSH, Shiu HYK, Ho KKS, Koo RCH (2014) Physical modelling of baffles influence on landslide debris mobility. Landslides 12(1):1–18
Owen MW, Steele AAJ (1991) HR Wallingford, Report SR 261: Effectiveness of recurve wave return walls. Wallingford, UK
Rapaport DC (2004) The art of molecular dynamic simulation, 2nd edn. Cambridge University Press, New York
Robotham ME, Wang H, Walton G (1995) Assessment of the risk from rock fall from active and abandoned quarry slopes. Transactions of the Institute of Mining and Metallurgy (Section A) 104:25–33
Savage SB (1984) The mechanics of rapid granular flows. Adv Appl Mech 24:289–366
Schoones T (2014) Impermeable recurve seawalls to reduce wave overtopping. MEng thesis, Stollenbosch University
Shan T, Zhao JD (2014) A coupled CFD-DEM analysis of granular flow impacting on water reservoir. Acta Mech 225(8):2449–2470
Stanier SA, Blaber J, Take WA, White DJ (2015) Improved image-based deformation measurement for geotechnical applications. Can Geotech J 53:1–13
Teufelsbauer H, Wang Y, Chiou M-C, Wu W (2009) Flow-obstacle-interaction in rapid granular avalanches: DEM simulation and comparison with experiment. Granul Matter 11(4):209–200
Teufelsbauer H, Wang Y, Pudasaini SP, Borja RI, Wu W (2011) DEM simulation of impact force exerted by granular flow on rigid structures. Acta Geotech 6(3):119–133
Valentino R, Barla G, Montrasio L (2008) Experimental analysis and micromechanical modelling of dry granular flow and impacts in laboratory flume tests. Rock Mech Rock Eng 41(1):153–177
Verwaest T, Vanpoucke P, Willems M, De Mulder T (2010) Waves overtopping a wide-crested dike. In: Proc 32nd Int Conf Coastal Engineering. 30 June - 5 July 2010. ICCE, Shanghai, pp 1–9
White DJ, Take WA, Bolton MD (2003) Soil deformation measurement using particle image velocimetry (PIV). Géotechnique 53(7):619–631
Wei F, Yang H, Hu K, Hong Y, Li X (2012) Two methods for measuring internal velocity of debris flows in the laboratory. In: Monitoring, simulation, prevention and remediation of dense and debris flows IV
Zhao J, Shan T (2013) Coupled CFD-DEM simulation of fluid-particle interaction in geomechanics. Powder Technol 239:248–258
Zhou GGD, Ng CWW (2010) Numerical investigation of reverse segregation in debris flows by DEM. Gran Matter 12(5):507–516

C. W. W. Ng · C. E. Choi (✉) · G. R. Goodwin · W. W. Cheung
Department of Civil Engineering,
Hong Kong University of Science and Technology,
Clear Water Bay, Kowloon, Hong Kong
e-mail: ceclarence@ust.hk

C. E. Choi
HKUST Jockey Club Institute for Advanced Study,
Hong Kong University of Science and Technology,
Clear Water Bay, Kowloon, Hong Kong